

Vela pulsar wind nebula X-rays are polarized to near the synchrotron limit

<https://doi.org/10.1038/s41586-022-05476-5>

Received: 12 June 2022

Accepted: 24 October 2022

Published online: 21 December 2022

 Check for updates

Fei Xie^{1,2}, Alessandro Di Marco², Fabio La Monaca², Kuan Liu¹, Fabio Muleri², Niccolò Bucciantini^{3,4,5}, Roger W. Romani^{6,7}, Enrico Costa², John Rankin², Paolo Soffitta², Matteo Bachetti⁸, Niccolò Di Lalla^{6,7}, Sergio Fabiani², Riccardo Ferrazzoli², Shuichi Gunji⁹, Luca Latronico¹⁰, Michela Negro^{11,12,13}, Nicola Omodei^{6,7}, Maura Pilia⁸, Alessio Trois⁸, Eri Watanabe⁹, Iván Agudo¹⁴, Lucio A. Antonelli^{15,16}, Luca Baldini^{17,18}, Wayne H. Baumgartner¹⁹, Ronaldo Bellazzini¹⁷, Stefano Bianchi²⁰, Stephen D. Bongiorno¹⁹, Raffaella Bonino^{10,21}, Alessandro Brez¹⁷, Fiamma Capitanio², Simone Castellano¹⁷, Elisabetta Cavazzuti²², Stefano Ciprini^{16,23}, Alessandra De Rosa², Ettore Del Monte², Laura Di Gesu²², Immacolata Donnarumma²², Victor Doroshenko²⁴, Michal Dovčiak²⁵, Steven R. Ehlert¹⁹, Teruaki Enoto²⁶, Yuri Evangelista², Javier A. Garcia²⁷, Kiyoshi Hayashida^{28,51}, Jeremy Heyl²⁹, Wataru Iwakiri³⁰, Svetlana G. Jorstad^{31,32}, Vladimir Karas²⁵, Takao Kitaguchi²⁶, Jeffery J. Kolodziejczak¹⁹, Henric Krawczynski^{33,34}, Ioannis Liodakis³⁵, Simone Maldera¹⁰, Alberto Manfreda¹⁷, Frédéric Marin³⁶, Andrea Marinucci²², Alan P. Marscher³¹, Herman L. Marshall³⁷, Francesco Massaro^{10,21}, Giorgio Matt²⁰, Ikuyuki Mitsuishi³⁸, Tsunefumi Mizuno³⁹, C.-Y. Ng⁴⁰, Stephen L. O'Dell¹⁹, Chiara Oppedisano¹⁰, Alessandro Papitto¹⁵, George G. Pavlov⁴¹, Abel L. Peirson^{6,7}, Matteo Perri^{15,16}, Melissa Pesce-Rollins¹⁷, Pierre-Olivier Petrucci⁴², Andrea Possenti⁸, Juri Poutanen^{43,44}, Simonetta Puccetti²², Brian D. Ramsey¹⁹, Ajay Ratheesh², Carmelo Sgró¹⁷, Patrick Slane⁴⁵, Gloria Spandre¹⁷, Toru Tamagawa²⁶, Fabrizio Tavecchio⁴⁶, Roberto Taverna⁴⁷, Yuzuru Tawara³⁸, Allyn F. Tenant¹⁹, Nicolas E. Thomas¹⁹, Francesco Tombesi⁴⁸, Sergey S. Tsygankov^{43,44}, Roberto Turolla^{47,49}, Jacco Vink⁵⁰, Martin C. Weisskopf¹⁹, Kinwah Wu⁴⁹ & Silvia Zane⁴⁹

Pulsar wind nebulae are formed when outflows of relativistic electrons and positrons hit the surrounding supernova remnant or interstellar medium at a shock front. The Vela pulsar wind nebula is powered by a young pulsar (B0833-45, aged 11,000 years)¹ and located inside an extended structure called Vela X, which is itself inside the supernova remnant². Previous X-ray observations revealed two prominent arcs that are bisected by a jet and counter jet^{3,4}. Radio maps have shown high linear polarization of 60% in the outer regions of the nebula⁵. Here we report an X-ray observation of the inner part of the nebula, where polarization can exceed 60% at the leading edge—approaching the theoretical limit of what can be produced by synchrotron emission. We infer that, in contrast with the case of the supernova remnant, the electrons in the pulsar wind nebula are accelerated with little or no turbulence in a highly uniform magnetic field.

The Imaging X-ray Polarimetry Explorer (IXPE)^{6,7} provides an X-ray view of the highest-energy electrons near their acceleration sites. IXPE is a NASA–Italian Space Agency (ASI) explorer featuring three co-aligned X-ray telescopes each with an imaging photoelectric polarimeter detector unit based on a gas pixel detector^{8,9}. IXPE observed the Vela pulsar wind nebula (PWN) in two periods—(1) 5 April 2022 to 15 April 2022 and (2) 21 April 2022 to 30 April 2022—with a total exposure of 860 ks. The data were extracted from the publicly available files processed by the IXPE Science Operations Center and analysed using standard tools as described in the Supplementary Methods.

Linear polarization is detected at high significance (-31σ) for the spatial- and energy-integrated Vela PWN in the 2–8 keV band. The linear polarization degree (PD) is $44.6 \pm 1.4\%$ with a polarization angle

(PA, also known as electric vector position angle EVPA, defined from north to east) of $-50.0 \pm 0.9^\circ$, with 68.3% confidence level uncertainties. Previously, only the Crab PWN has been studied by X-ray polarization; the classic 1976 and 1978 OSO-8 results^{10,11} have recently been confirmed by the Polarlight cube-sat¹². However, these observations provided only an integrated polarization measurement and the image-averaged PD was less than half of that found here for Vela.

IXPE's imaging abilities, with a $\leq 30''$ half-power diameter⁷, enable a spatially resolved polarimetric measurement of the PWN (Fig. 1). Here, 25 independent $30'' \times 30''$ square regions were analysed, combining data from the three detector units. The pulsar and compact arc-jet structure lie largely within the central region. The pulsar, dominated by a $kT \approx 0.13$ keV thermal component¹³, contributes less than 10% of the

A list of affiliations appears at the end of the paper.

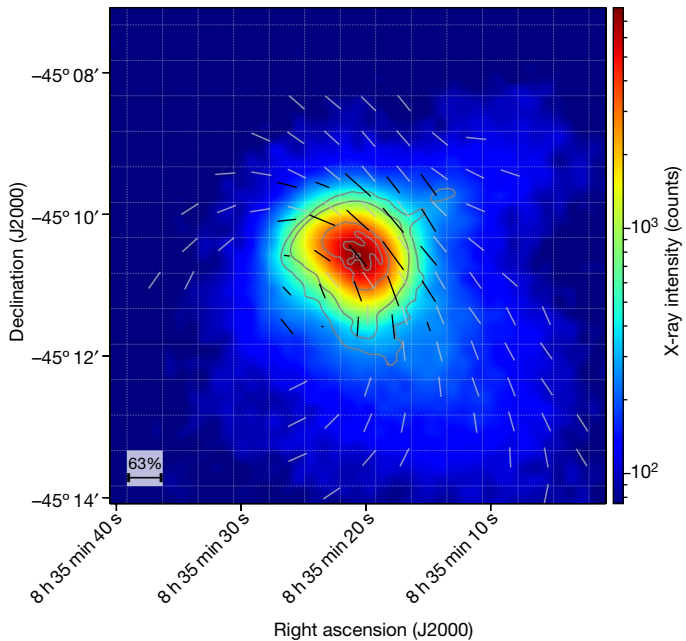


Fig. 1 | The IXPE intensity map of the Vela PWN in the 2–8 keV range with the measured X-ray polarization and radio polarization vectors overlaid. The intensity is the Gaussian-smoothed sum of the three detector units. The black lines present the X-ray polarization in the corresponding $30'' \times 30''$ image elements (white grids), their lengths indicate the PD and the orientation indicates the projected magnetic field (90° from the EVPA). The thinner silver lines, drawn with the same lengths, show the 5 GHz polarization directions derived from ref.⁵. The grey contours, obtained from Chandra observations in the same 2–8 keV range, give a better illustration of the pulsar, compact arc-jet structure, diffuse emission shell and relatively weak outer jet (only weakly detected at IXPE resolution). The bar at the bottom left presents the maximum measured X-ray PD of 63%, and the PD and PA in each of 25 grids are provided in Extended Data Table 3.

IXPE counts in this region. IXPE has not measured the polarization of the pulsed source; this may add to or subtract from the nebular polarization but, with the low flux (and low expected PD¹⁴), the effect should be small. The black lines show linear polarization, with the line length indicating a PD of up to 62.8%. These lines are at 90° to the EVPA and therefore show the direction of the projected magnetic field, which is highly symmetric about the pulsar jet axis.

The curved and symmetric PA pattern seen in Fig. 1 implies that there will be some PA variation across, and decrease in the region-average PD of, our 25 measurement regions. This is most obvious to the sides and rear of the PWN, where the arcs seen in the Chandra image are highly curved and, therefore, the underlying PA varies rapidly, producing substantial depolarization. As the polarization follows the Chandra X-ray morphology, we expect slightly higher PD and smaller errors in regions in which the arcs are less curved, which enables us to average over larger areas. For example, a morphologically selected region at the front of the nebula along the symmetry axis provides a $PD = 70.0 \pm 3.6\%$ (Methods and Extended Data Fig. 5). As a caution, we note that, for an analysis near the angular resolution limit in regions covering sharp intensity gradients, an effect due to the reconstruction of the photo-electron tracks in the gas pixel detector can artificially alter the local polarization values. Monte Carlo analysis shows that this is a $\lesssim 5\%$ effect, with a slight decrease in PD to the north and increase to the south; our maximally polarized zones are hardly affected. Regardless, Vela's high PD and symmetric pattern imply a highly ordered magnetic field following the PWN's toroidal structure.

The spatially averaged polarization of the Vela PWN is plotted as a function of energy in Fig. 2. A slight increase in PD with energy is seen. This

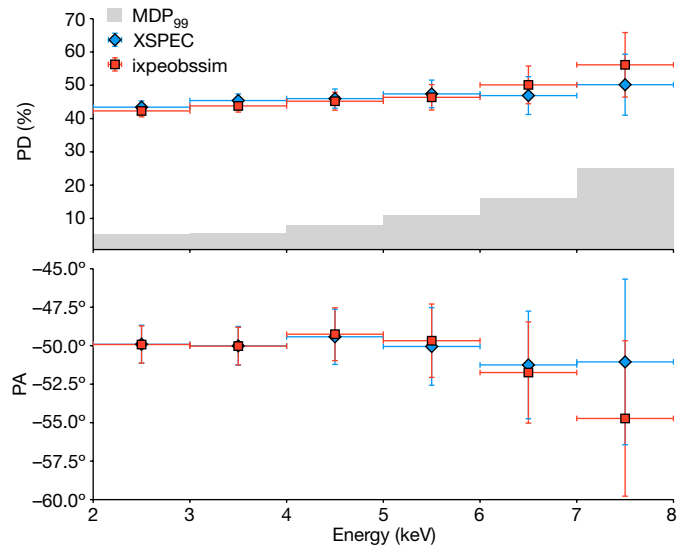


Fig. 2 | Image-average polarization of the Vela PWN as a function of energy. PD (top) and PA (bottom) were derived using ixpeobssim (red) and XSPEC (blue) independently. The results are from the joint analysis of three detector units with uncertainties calculated at a 68.3% confidence level. PD values in all of the energy bins are significantly higher than the minimum detectable polarization at the 99% confidence level (MDP₉₉), shown as a grey histogram.

might be expected, as the emission region shrinks with increasing energy, therefore arising from a smaller range of magnetic field orientations. The image-averaged PA does not show significant energy dependence.

It is widely accepted that PWN arc-jet structures are due to an anisotropic pulsar wind, which generates toroidal magnetic fields in the equatorial zone^{15–18}. In this picture, the integrated PA should align with the symmetry axis of the Vela PWN^{19–21}, consistent with the results reported here. The non-thermal radio and X-ray spectra of the Vela PWN already indicated domination by synchrotron emission. The high linear X-ray polarization, measured here using IXPE, strengthens this conclusion.

The maximum PD of synchrotron radiation from a power law spectrum of electrons with index p in a uniform magnetic field is $\Pi = (p + 1)/(p + 7/3)$ (ref.²²); the photon index Γ of the emitted radiation is given by $p = 2\Gamma - 1$. For Vela, with $\Gamma = 1.3 \pm 0.04$ in the compact jet-arc structure, increasing to 1.7 in the outskirts²³, the maximum PD is 66–72%. Thus, the 62.8% seen in Fig. 1 and Extended Data Table 3 (or the 70% in the regions selected according to the Chandra image in Extended Data Table 4) is quite close to the maximum permitted value. This implies a magnetic field that is highly uniform across the measured region, with little turbulence-induced fluctuations. Moreover, $\Gamma = 1.3$ implies $p = 1.6$, appreciably flatter than the $p \approx 2.3\text{--}2.6$ of turbulent diffusive shock acceleration²⁴; another mechanism, such as reconnection²⁵, should have a dominant role in PWN particle energization.

The high uniformity and toroidal magnetic structure that we see with IXPE evidently extends to larger radii, where the linear polarization of the $4'$ radio lobes indicates a magnetic field with a similar symmetry axis⁵ (Fig. 1). Interestingly, this magnetic structure is compressed to the north (evidently by the PWN interaction with the larger supernova remnant) and has a larger radius of curvature, centred behind the pulsar. With little radio emission from the X-ray bright torus/jet zone in the centre, it appears that the radio tracks an older, cooler electron population centred behind the pulsar and extending to larger radii. Still, the substantial radio polarization, reaching 60% at both 5 GHz (ref.⁵) and 1.4 GHz (ref.²⁶), indicates that the ordered and minimally turbulent fields probed by IXPE extend into this radio-emitting zone at much larger radii.

At present, we can say little about the X-ray polarization from the pulsar itself. Much deeper observations (and probably at a higher

spatial resolution) will be required to isolate this component and compare with the optical phase average polarization of $\text{PD} = 8.1 \pm 0.6\%$ at $\text{PA} = 146.3 \pm 2.4^\circ$ (ref. ²⁷). Like the Crab pulsar, Vela's average optical PA lies close to the projected torus axis. If, like the Crab pulsar, the phase-average X-ray PD is well below that of the optical emission, corrections to our nebular estimates will be very small.

We found a notable high X-ray polarization in the Vela PWN, reaching an image- and energy-averaged PD of about 45%. The non-thermal PWN spectrum is bright in the IXPE energy band; the Vela pulsar itself emits mostly soft thermal X-rays that are too faint and weakly polarized for detection at present. Our IXPE image sufficiently resolves the PWN to show that the polarization structure is symmetric about the projected pulsar spin (and proper motion) axis; this symmetry extends in radio polarization studies to even larger angles. The varying PA across the nebula implies that the true local polarization is even greater and, indeed, we found PD values of $\geq 60\%$ for some regions. This is close to the maximum PD allowed for synchrotron emission with the observed X-ray spectrum, implying that the magnetic field is highly uniform across the emission region. As electrons emitting synchrotron X-rays cool very rapidly, the IXPE X-rays are emitted close to the acceleration zone. In turn this argues against turbulence-driven diffusive shock acceleration and suggests that other processes, such as reconnection, should energize the PWN particles in the termination shock. Further IXPE studies of Vela and other bright PWNe should connect the X-ray polarization pattern with the details of the compact structures, further probing the physics of relativistic shock acceleration.

Online content

Any methods, additional references, Nature Portfolio reporting summaries, source data, extended data, supplementary information, acknowledgements, peer review information; details of author contributions and competing interests; and statements of data and code availability are available at <https://doi.org/10.1038/s41586-022-05476-5>.

1. Caraveo, P. A., De Luca, A., Mignani, R. P. & Bignami, G. F. The distance to the Vela Pulsar gauged with Hubble Space Telescope parallax observations. *Astrophys. J.* **561**, 930–937 (2001).
2. Slane, P. et al. Investigating the structure of Vela X. *Astrophys. J.* **865**, 86 (2018).
3. Pavlov, G. G., Kargaltsev, O. Y., Sanwal, D. & Garmire, G. P. Variability of the Vela Pulsar wind nebula observed with Chandra. *Astrophys. J. Lett.* **554**, L189–L192 (2001).
4. Helfand, D. J., Gotthelf, E. V. & Halpern, J. P. Vela Pulsar and its synchrotron nebula. *Astrophys. J.* **556**, 380–391 (2001).
5. Dodson, R., Lewis, D., McConnell, D. & Deshpande, A. A. The radio nebula surrounding the Vela pulsar. *Mon. Not. R. Astron. Soc.* **343**, 116–124 (2003).
6. Soffitta, P. et al. The instrument of the Imaging X-ray Polarimetry Explorer. *Astron. J.* **162**, 208 (2021).
7. Weisskopf, M. C. et al. The Imaging X-ray Polarimetry Explorer (IXPE): pre-launch. *J. Astron. Telesc. Instrum. Syst.* **8**, 026002 (2022).
8. Costa, E. et al. An efficient photoelectric x-ray polarimeter for the study of black holes and neutron stars. *Nature* **411**, 662–665 (2001).
9. Baldini, L. et al. Design, construction, and test of the Gas Pixel Detectors for the IXPE mission. *Astropart. Phys.* **133**, 102628 (2021).
10. Weisskopf, M. C. et al. Measurement of the X-ray polarization of the Crab Nebula. *Astrophys. J. Lett.* **208**, L125–L128 (1976).
11. Weisskopf, M. C., Silver, E. H., Kestenbaum, H. L., Long, K. S. & Novick, R. A precision measurement of the X-ray polarization of the Crab Nebula without pulsar contamination. *Astrophys. J. Lett.* **220**, L117–L121 (1978).
12. Feng, H. et al. Re-detection and a possible time variation of soft X-ray polarization from the Crab. *Nat. Astron.* **4**, 511–516 (2020).
13. Pavlov, G. G., Zavlin, V. E., Sanwal, D., Burwitz, V. & Garmire, G. P. The X-ray spectrum of the Vela Pulsar resolved with the Chandra X-ray observatory. *Astrophys. J. Lett.* **552**, L129–L133 (2001).
14. Bucciantini, N. et al. Simultaneous space and phase resolved X-ray polarimetry of the Crab Pulsar and Nebula. Preprint at arXiv <https://arxiv.org/abs/2207.05573> (2022).
15. Ng, C. Y. & Romani, R. W. Fitting pulsar wind tori. *Astrophys. J.* **601**, 479–484 (2004).
16. Lyubarsky, Y. E. On the structure of the inner Crab Nebula. *Mon. Not. R. Astron. Soc.* **329**, L34–L36 (2002).
17. Komissarov, S. S. & Lyubarsky, Y. E. The origin of peculiar jet-torus structure in the Crab nebula. *Mon. Not. R. Astron. Soc.* **344**, L93–L96 (2003).
18. Del Zanna, L., Amato, E. & Bucciantini, N. Axially symmetric relativistic MHD simulations of pulsar wind nebulae in supernova remnants. On the origin of torus and jet-like features. *Astron. Astrophys.* **421**, 1063–1073 (2004).
19. Komissarov, S. S. & Lyubarsky, Y. E. Synchrotron nebulae created by anisotropic magnetized pulsar winds. *Mon. Not. R. Astron. Soc.* **349**, 779–792 (2004).
20. Bucciantini, N., del Zanna, L., Amato, E. & Volpi, D. Polarization in the inner region of pulsar wind nebulae. *Astron. Astrophys.* **443**, 519–524 (2005).
21. Del Zanna, L., Volpi, D., Amato, E. & Bucciantini, N. Simulated synchrotron emission from pulsar wind nebulae. *Astron. Astrophys.* **453**, 621–633 (2006).
22. Rybicki, G. B. & Lightman, A. P. *Radiative Processes in Astrophysics* (Wiley, 1986).
23. Kargaltsev, O., Pavlov, G. G., Sanwal, D. & Garmire, G. P. in *Neutron Stars in Supernova Remnants* Vol. 271 (eds Slane, P. O. & Gaensler, B. M.) 181 (Astronomical Society of the Pacific, 2002).
24. Sironi, L., Keshet, U. & Lemoine, M. Relativistic shocks: particle acceleration and magnetization. *Space Sci. Rev.* **191**, 519–544 (2015).
25. Sironi, L. & Spitkovsky, A. Relativistic reconnection: an efficient source of non-thermal particles. *Astrophys. J. Lett.* **783**, L21 (2014).
26. Bock, D. C. J., Sault, R. J., Milne, D. K. & Green, A. J. in *Neutron Stars in Supernova Remnants* Vol. 271 (eds Slane, P. O. & Gaensler, B. M.) 187 (Astronomical Society of the Pacific, 2002).
27. Moran, P., Mignani, R. P. & Shearer, A. HST optical polarimetry of the Vela pulsar and nebula. *Mon. Not. R. Astron. Soc.* **445**, 835–844 (2014).

Publisher's note Springer Nature remains neutral with regard to jurisdictional claims in published maps and institutional affiliations.

Springer Nature or its licensor (e.g. a society or other partner) holds exclusive rights to this article under a publishing agreement with the author(s) or other rightsholder(s); author self-archiving of the accepted manuscript version of this article is solely governed by the terms of such publishing agreement and applicable law.

© The Author(s), under exclusive licence to Springer Nature Limited 2022

¹Guangxi Key Laboratory for Relativistic Astrophysics, School of Physical Science and Technology, Guangxi University, Nanning, China. ²INAF Istituto di Astrofisica e Planetologia Spaziali, Rome, Italy. ³INAF Osservatorio Astrofisico di Arcetri, Florence, Italy. ⁴Dipartimento di Fisica e Astronomia, Università degli Studi di Firenze, Florence, Italy. ⁵Istituto Nazionale di Fisica Nucleare, Sezione di Firenze, Florence, Italy. ⁶Department of Physics, Stanford University, Stanford, CA, USA. ⁷Kavli Institute for Particle Astrophysics and Cosmology, Stanford University, Stanford, CA, USA. ⁸INAF Osservatorio Astronomico di Cagliari, Cagliari, Italy. ⁹Yamagata University, Yamagata, Japan. ¹⁰Istituto Nazionale di Fisica Nucleare, Sezione di Torino, Torino, Italy. ¹¹NASA Goddard Space Flight Center, Greenbelt, MD, USA. ¹²University of Maryland, Baltimore County, Baltimore, MD, USA. ¹³Center for Research and Exploration in Space Science and Technology, NASA/GSFC, Greenbelt, MD, USA. ¹⁴Instituto de Astrofísica de Andalucía—CSIC, Granada, Spain. ¹⁵INAF Osservatorio Astronomico di Roma, Monte Porzio Catone (RM), Italy. ¹⁶Space Science Data Center, Agenzia Spaziale Italiana, Rome, Italy. ¹⁷Istituto Nazionale di Fisica Nucleare, Sezione di Pisa, Pisa, Italy. ¹⁸Dipartimento di Fisica, Università di Pisa, Pisa, Italy. ¹⁹NASA Marshall Space Flight Center, Huntsville, AL, USA. ²⁰Dipartimento di Matematica e Fisica, Università degli Studi Roma Tre, Rome, Italy. ²¹Dipartimento di Fisica, Università degli Studi di Torino, Torino, Italy. ²²Agenzia Spaziale Italiana, Rome, Italy. ²³Istituto Nazionale di Fisica Nucleare, Sezione di Roma Tor Vergata, Rome, Italy. ²⁴Institut für Astronomie und Astrophysik, Tübingen, Germany. ²⁵Astronomical Institute of the Czech Academy of Sciences, Prague, Czech Republic. ²⁶RIKEN Cluster for Pioneering Research, Wako, Japan. ²⁷California Institute of Technology, Pasadena, CA, USA. ²⁸Osaka University, Suita, Osaka, Japan. ²⁹University of British Columbia, Vancouver, British Columbia, Canada. ³⁰Department of Physics, Faculty of Science and Engineering, Chuo University, Tokyo, Japan. ³¹Institute for Astrophysical Research, Boston University, Boston, MA, USA. ³²Laboratory of Observational Astrophysics, St Petersburg University, St Petersburg, Russia. ³³Physics Department, Washington University in St Louis, St Louis, MO, USA. ³⁴McDonnell Center for the Space Sciences, Washington University in St Louis, St Louis, MO, USA. ³⁵Finnish Centre for Astronomy with ESO, University of Turku, Turku, Finland. ³⁶Université de Strasbourg, CNRS, Observatoire Astronomique de Strasbourg, Strasbourg, France. ³⁷MIT Kavli Institute for Astrophysics and Space Research, Massachusetts Institute of Technology, Cambridge, MA, USA. ³⁸Graduate School of Science, Division of Particle and Astrophysical Science, Nagoya University, Nagoya, Japan. ³⁹Hiroshima Astrophysical Science Center, Hiroshima University, Hiroshima, Japan. ⁴⁰Department of Physics, University of Hong Kong, Pokfulam, Hong Kong. ⁴¹Department of Astronomy and Astrophysics, Pennsylvania State University, University Park, PA, USA. ⁴²Université Grenoble Alpes, CNRS, IPAG, Grenoble, France. ⁴³Department of Physics and Astronomy, University of Turku, Turku, Finland. ⁴⁴Space Research Institute of the Russian Academy of Sciences, Moscow, Russia. ⁴⁵Center for Astrophysics, Harvard & Smithsonian, Cambridge, MA, USA. ⁴⁶INAF Osservatorio Astronomico di Brera, Merate, Italy. ⁴⁷Dipartimento di Fisica e Astronomia, Università degli Studi di Padova, Padova, Italy. ⁴⁸Dipartimento di Fisica, Università degli Studi di Roma Tor Vergata, Rome, Italy. ⁴⁹Mullard Space Science Laboratory, University College London, Dorking, UK. ⁵⁰Anton Pannekoek Institute for Astronomy & GRAPPA, University of Amsterdam, Amsterdam, The Netherlands. ⁵¹Deceased: Kiyoshi Hayashida. [✉]e-mail: xief@gxu.edu.cn

Methods

IXPE data analysis

This work is based on the polarimetric observations of the Vela pulsar and nebula obtained with the IXPE—a NASA mission in partnership with the ASI as described previously^{6,7} and the references therein. The IXPE Observatory includes three identical X-ray telescopes, each comprising an X-ray mirror assembly and a linear-polarization-sensitive detector, and performs imaging polarimetry over a nominal 2–8 keV energy band. IXPE data are telemetered to ground stations in Malindi (primary) and in Singapore (secondary), and are transmitted to the NASA Marshall Space Flight Center Science Operations Center (SOC) through the Mission Operations Center at the Laboratory for Atmospheric and Space Physics, University of Colorado. Data are processed at the SOC, where raw data and relevant engineering/ancillary data are used to produce photon event lists. For each observation, the data are archived at the High Energy Astrophysics Science Archive Research Center (HEASARC), at the NASA Goddard Space Flight Center for use by the international astrophysics community.

IXPE data are provided in two levels/formats: event_l1 and event_l2. The first level consists of unfiltered events; event_l2 files are produced from event_l1 after further calibration/correction procedures. In particular, event_l2 data are cleaned of in-flight calibration data and occultation/SAA passages, then energy calibration/equalization of the three detector units (DUs) is applied and Stokes parameters are estimated as described previously²⁸. After this the spurious modulation is removed²⁹ and the photons are referenced to sky coordinates, removing dithering pattern and boom motion effects.

The Vela pulsar and PWN were observed with the IXPE from 5 April 2022 at 19:51:40.687 UTC to 15 April 2022 at 18:08:18.343 UTC, and again from 21 April 2022 at 12:22:11.549 UTC to 30 April 2022 at 10:34:51.991 UTC, with net exposures 860 ks, 854 ks and 868 ks, respectively for the three DUs. After retrieving event_l2 files from the HEASARC, we performed three corrections: (1) energy correction (based on the onboard calibration data); (2) bad time interval filtering (to remove the solar flare events; Extended Data Fig. 1); (3) barycentre correction (to convert the photon arrival time into the solar system barycentre; done using the standard HEASoft (v.6.30.1) barycorr, with the following options: refframe=ICRS, ephem=JPLEPH.421). We found that the IXPE Vela observations were slightly affected by an increased particle flux during some portions of the orbit that are associated with high solar activity. Bad time intervals are identified as periods with count rates 3σ higher than average, assuming a Gaussian distribution. Events during such bad intervals were excluded from further data analysis.

The field of view of each detector is $12.9' \times 12.9'$ (with the three detectors mounted at angles of 120° to each other)⁷, while the X-ray emission of Vela PWN covers a much smaller region³. We identified source and background regions using the SAOImageDS9 software³⁰. The source region is a circle of radius 1' centred on the pulsar. The background region is an annulus with inner radius of 2' and an outer radius of 4.7' (Extended Data Fig. 2).

The polarization data consist of Stokes parameters (I, Q, U) for each photon in the event_12 files. For details on the Stokes parameters as defined in IXPE data see ref. ³¹. Data analysis was performed using different techniques and by different groups within the IXPE collaboration to cross-check the results. We first analysed the data using the IXPE internal software ixpeobssim³², customized for IXPE data analysis and simulations. ixpeobssim includes tools developed to determine the source polarization properties through an analysis independent of the spectral models, according to the unbinned method described previously²⁸. A second reduction was performed with XSPEC, using HEASoft (v.6.30.1), which includes models for spectropolarimetric analysis³³. With the binned spectra of the Stokes parameters, XSPEC performs standard forward-fitting and derives model-dependent polar-

ization parameters. The adopted IXPE response functions are from the HEASARC IXPE CALDB 14 March 2022 release.

The spectral analysis shows that background events are not negligible at high energies, with rates becoming comparable (Extended Data Fig. 3). To determine the source polarization while avoiding dilution effects at high energies, the background component was subtracted in all of the analyses. The 2–8 keV band-averaged, aperture-averaged (1' radius) PD and PA measurements are summarized in Extended Data Table 1. The results are consistent between the three DUs and the two different analysis methods.

Spectropolarimetric analysis was performed using XSPEC³⁴ to jointly fit the three DUs in a two-step procedure. In the first step, the $/$ energy distribution is fitted with a spectral model. In the second step the spectral model is fixed, while U and Q are fit. Thus, this method does a forward folding fit to the binned spectra of the Stokes parameters I , Q and U jointly after fixing the spectral model.

The Vela PWN binned $/$ spectra from the three DUs were fitted with the model FACTOR \times TBABS \times POWERLAW, where TBABS takes into account the interstellar absorption. Here we fixed the column density¹³ to $N_H = 0.03 \times 10^{22} \text{ cm}^{-2}$ —a relative normalization factor for DU2 and DU3 accounts for uncertainties in their absolute effective area. The best-fit curves and the spectra of the Vela PWN for the three DUs are shown in Extended Data Fig. 3. At present, uncertainties in the effective area energy dependence are substantial, due to the incomplete knowledge of telescope alignment and related vignetting. Accordingly, we focus on the polarization information. The spectral model parameters do not affect the polarization results, which are affected only by the energy assigned to individual photons. The individual photon energy estimate is tied to frequent in-flight calibration, performed by an onboard calibration source during the Earth occultation. As the effective area variation becomes better understood, we expect the spectral model fitting to improve.

With the spectral model, binned I , Q and U spectra are fitted to obtain the polarimetric information, using the polarization model POLCONST of XSPEC. The fitted I , Q , U spectra in the 2–8 keV energy band are shown in Extended Data Fig. 3. The PA and PD obtained are in good agreement with those obtained by the model-independent analysis performed using ixpeobssim, as reported in Extended Data Table 1.

The same procedure was used to investigate the polarization in six energy bins fitting with XSPEC model FACTOR \times TBABS \times POWERLAW \times POLCONST in each energy interval, freezing the $/$ spectral model parameters to the values previously obtained from the 2–8 keV analysis. The PD and PA in each energy bin are reported in Fig. 2 and Extended Data Table 1. The ixpeobssim analysis is fully in agreement with that of XSPEC. PD and PA values obtained with XSPEC are represented in a 2D polar plot—with contours enclosing the 68.3% confidence levels—in Extended Data Fig. 4. Similarly, Q/I and U/I Stokes parameters obtained with XSPEC and ixpeobssim are shown in Extended Data Fig. 6.

We have attempted to quantify the significance of the $\text{PD}(E)$ trend in Fig. 2. Although a χ^2 test found that a constant PD is acceptable at the 57% level, a run-test analysis accepted this hypothesis at only 7.7% and a Kolmogorov–Smirnov test at only 3.6%. By contrast, a linear $\text{PD}(E)$ model gives an acceptable χ^2 probability at the 98% level, the run-test statistic is allowed at 41% and a Kolmogorov–Smirnov test accepted the hypothesis at the 98% level. Thus, a linear model with slope $1.8 \times 10^{-2} \pm 0.9 \times 10^{-2} \text{ keV}^{-1}$, while not demanded by the data, is preferred over a simple constant PD model at the 2σ confidence level.

Spatially resolved analysis

Spatially resolved analysis was performed using ixpeobssim. We divided the field of view into $30''$ square bins, guided by the mirror PSF. Polarization analysis was performed for each bin, without background subtraction. Removing the background counts would give a small increase in the PD without affecting the PA. The statistics in the outer bins are poor, so we present only the results in 5×5 grids centred on the pulsar (Fig. 1).

Article

The tabulated results of the normalized Q , U and their significance are provided in Extended Data Table 2, and the corresponding PD and PA are presented in Extended Data Table 3.

We also analysed the polarization parameters in five larger regions, aligned to the PWN symmetry axis, labelled L , R , F , B and C in Extended Data Fig. 5. Here we used ixpeobssim and subtracted a scaled off-source background. The results, tabulated in Extended Data Table 4, show a PD degree increasing along the symmetry axis from around 30% (B region) up to about 70% (F region). As with the finer square grid, L and R side regions show PA symmetrically spread about PA for the symmetry axis region C .

The effect of the pulsar on the PWN polarization

The X-rays of the 89 ms Vela pulsar are largely thermal and make a negligible contribution to the 2–8 keV PWN flux as a whole. Thus, they cannot notably affect our image-averaged PD and PA. However, from high-resolution Chandra images, we see that the pulsar contributes around 10% of the 2–8 keV flux in the central square region of Fig. 1 and it might therefore affect its polarization. To bound such effects, we measured the spectrum of the Vela pulsar using the Chandra observation obsid 218, processed through the standard pipeline using the CIAO (v.4.13) package and CALDB (v.4.9.5). If the pulsar contributes an unpolarized background, the corrected nebula-only PD rises to 55%. By contrast, if the pulsar emission is 100% polarized parallel (perpendicular) to the PA measured for the central square region, then the pulsar-subtracted polarization falls (rises) to 39% (66%). These values are from DU1 measurements only as, with the smallest half-power width, the pulsar will be most severe for this DU. In practice, the pulsar polarization is quite low in the optical band ($PD = 8.1 \pm 0.6\%$ at $PA = 146.3 \pm 0.6^\circ$)²⁷ and, by analogy with the Crab, will be even lower in the X-rays, so the true effect should be close to the unpolarized case, boosting the inferred PWN central PD. We apply this correction to the central bin in Fig. 1. Follow-up IXPE studies may more tightly bound the polarization of the pulsed emission.

Data availability

IXPE data are available through the NASA's HEASARC data archive (<https://heasarc.gsfc.nasa.gov>). Other derived data supporting the findings of this study are available from the corresponding author on request. Source data are provided with this paper.

Code availability

The High Energy Astrophysics Science Archive Research Center (HEASARC) developed the HEASOFT (HEASARC Software). We used the HEASOFT v.6.30.1 package for the spectropolarimetric IXPE data analysis, which is available online (<https://heasarc.gsfc.nasa.gov/docs/software/heasoft/>).

The proper instrument response functions are provided by the IXPE Team as a part of the IXPE calibration database released on 14 March 2022 and available in the HEASARC Calibration Database (https://heasarc.gsfc.nasa.gov/docs/heasarc/caldb/caldb_supported_missions.html). The software developed by IXPE collaboration is available publicly online (<https://ixpeobssim.readthedocs.io/en/latest/?badge=latest>). Information supporting the findings of this study is available from the corresponding author on request.

28. Kislat, F., Clark, B., Beilicke, M. & Krawczynski, H. Analyzing the data from X-ray polarimeters with Stokes parameters. *Astropart. Phys.* **68**, 45–51 (2015).
29. Rankin, J. et al. An algorithm to calibrate and correct the response to unpolarized radiation of the X-ray polarimeter onboard IXPE. *Astron. J.* **163**, 39 (2022).
30. Joye, W. A. in *Astronomical Data Analysis Software and Systems XV* Vol. 351 (eds Gabriel, C., Arviset, C., Ponz, D. & Enrique, S.) 574 (Astronomical Society of the Pacific, 2006).
31. Di Marco, A. et al. A weighted analysis to improve the X-ray polarization sensitivity of the imaging X-ray Polarimetry Explorer. *Astron. J.* **163**, 170 (2022).
32. Baldini, L. et al. ixpeobssim: A simulation and analysis framework for the imaging X-ray polarimetry explorer. *SoftwareX* **19**, 101194 (2022).
33. Strohmayer, T. E. X-ray spectro-polarimetry with photoelectric polarimeters. *Astrophys. J.* **838**, 72 (2017).
34. Arnaud, K. A. in *Astronomical Data Analysis Software and Systems V* Vol. 101 (eds Jacoby, G. H. & Barnes, J.) 17 (Astronomical Society of the Pacific, 1996).

Acknowledgements The IXPE is a joint US and Italian mission. The US contribution is supported by the National Aeronautics and Space Administration (NASA) and is led and managed by the Marshall Space Flight Center (MSFC), with industry partner Ball Aerospace (contract NNM15AA18C). The Italian contribution is supported by the Italian Space Agency (Agenzia Spaziale Italiana, ASI) through contract ASI-OHBI-2017-12-I-0, agreements ASI-INAF-2017-12-H0 and ASI-INFN-2017-13-H0, and its Space Science Data Center (SSDC) with agreements ASI-INAF-2022-14-HH-0 and ASI-INFN-2021-43-HH-0, and by the Istituto Nazionale di Astrofisica (INAF) and the Istituto Nazionale di Fisica Nucleare (INFN) in Italy. This research used data products provided by the IXPE Team (MSFC, SSDC, INAF and INFN) that are distributed with additional software tools by the High-Energy Astrophysics Science Archive Research Center (HEASARC), at NASA Goddard Space Flight Center (GSFC). The research at Guangxi University was supported in part by National Natural Science Foundation of China (grant no. 12133003). The research at Boston University was supported in part by National Science Foundation grant AST-2108622. I.A. acknowledges financial support from the Spanish ‘Ministerio de Ciencia e Innovación’ (MCINN) through the ‘Center of Excellence Severo Ochoa’ award for the Instituto de Astrofísica de Andalucía-CSIC (SEV-2017-0709) and through grants AYA2016-80889-P and PID2019-107847RB-C44.

Author contributions F.X. led the data analysis and the writing of the paper. A.D.M. and F.L.M. performed the spectropolarimetric analysis and contributed to the paper. F. Muleri and J.R. contributed to the data analysis and energy calibration of the dataset. K.L. and N.B. contributed to the data analysis and result interpretation. R.W.R. and L.L. helped to revise the manuscript. E. Costa, P. Soffitta, M.B., S.F., R.F., M. Pilia and A.T. contributed to the interpretation of the results and to text revisions. N.D.L., S.G., N.O., M.N. and E.W. performed independent analysis of the data. The other authors contributed to the design of the mission, to the calibration of the instrument, to the definition of its scientific case and to the planning of the observations. All of the authors provided inputs and comments on the manuscript.

Competing interests The authors declare no competing interests.

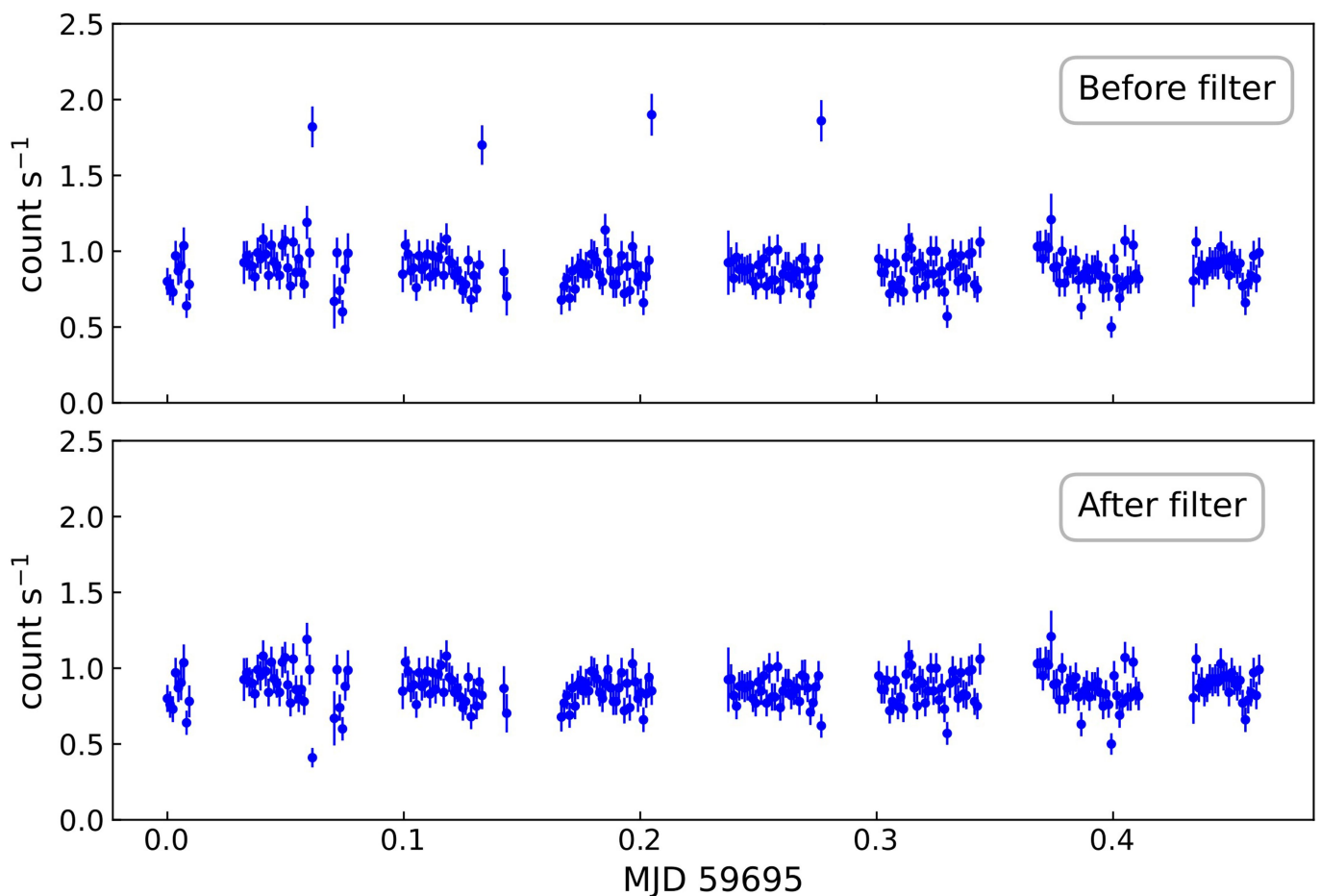
Additional information

Supplementary information The online version contains supplementary material available at <https://doi.org/10.1038/s41586-022-05476-5>.

Correspondence and requests for materials should be addressed to Fei Xie.

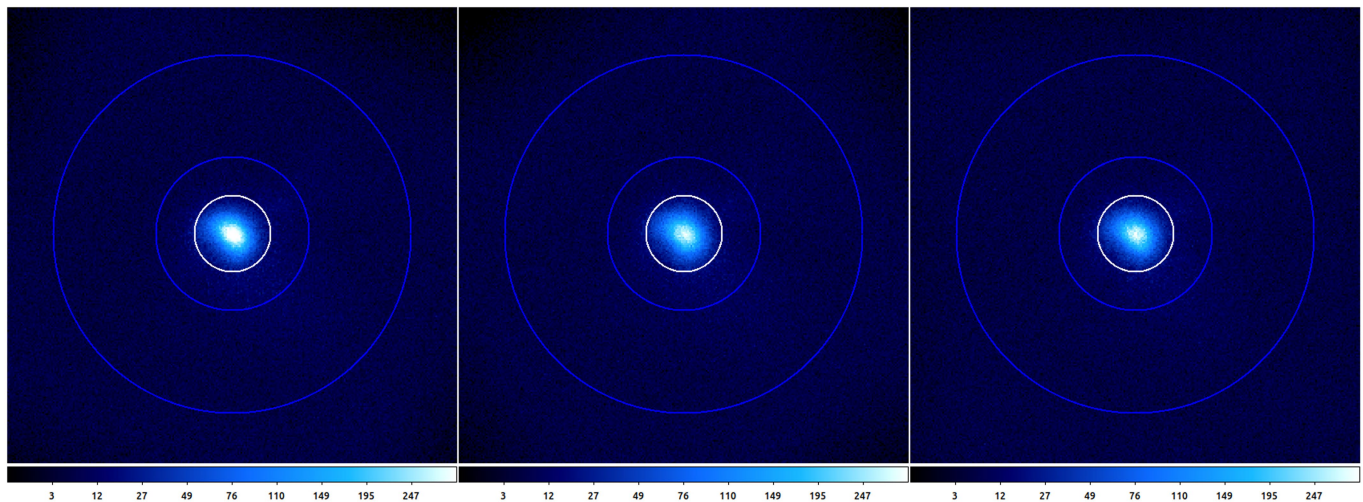
Peer review information *Nature* thanks the anonymous reviewers for their contribution to the peer review of this work.

Reprints and permissions information is available at <http://www.nature.com/reprints>.

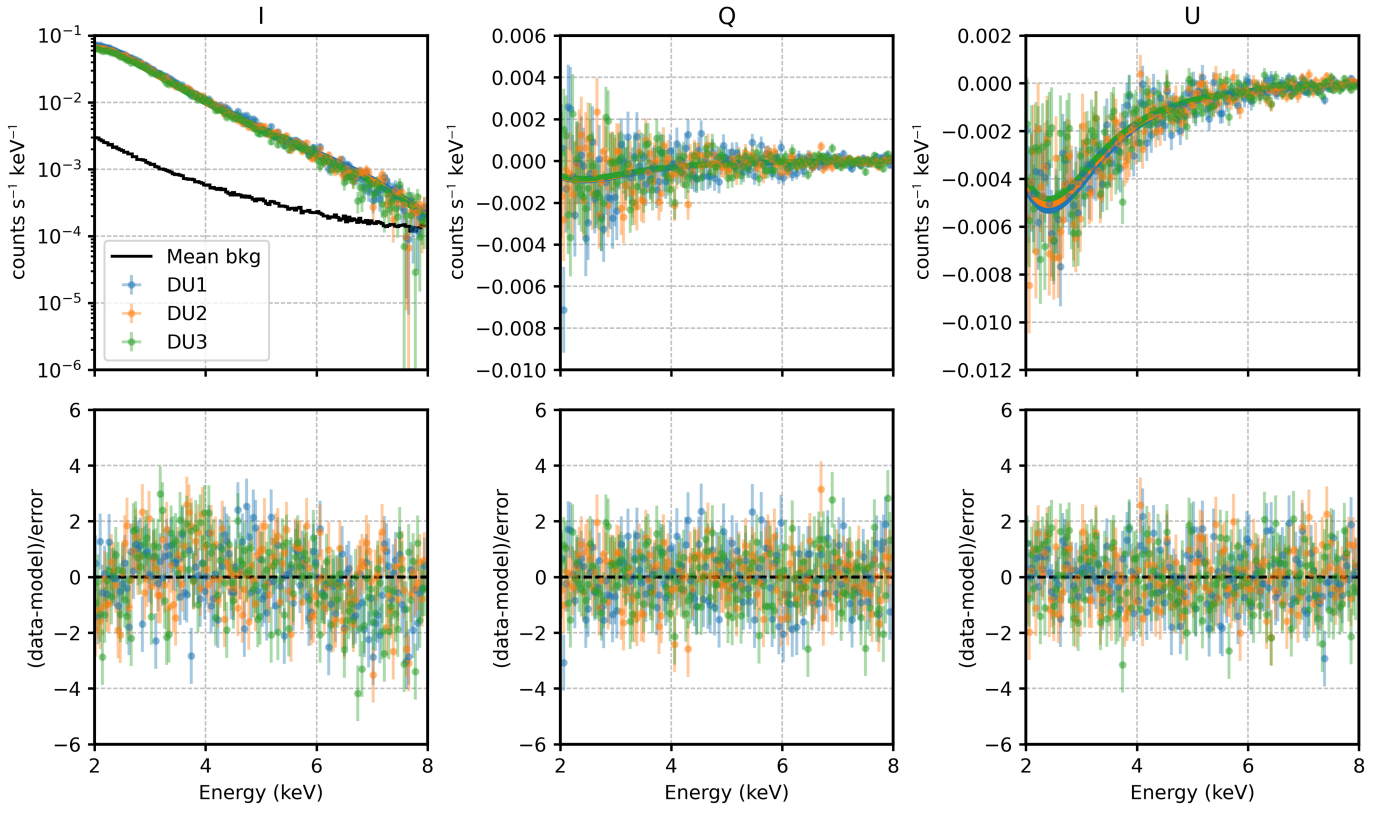


Extended Data Fig. 1 | Light curve of the Vela PWN observed by IXPE DU1 before and after data filtering (top and bottom panels, respectively). Filtering the high count-rate excursions from the event_J2 file removes approximately 1.47% of the exposure time.

Article

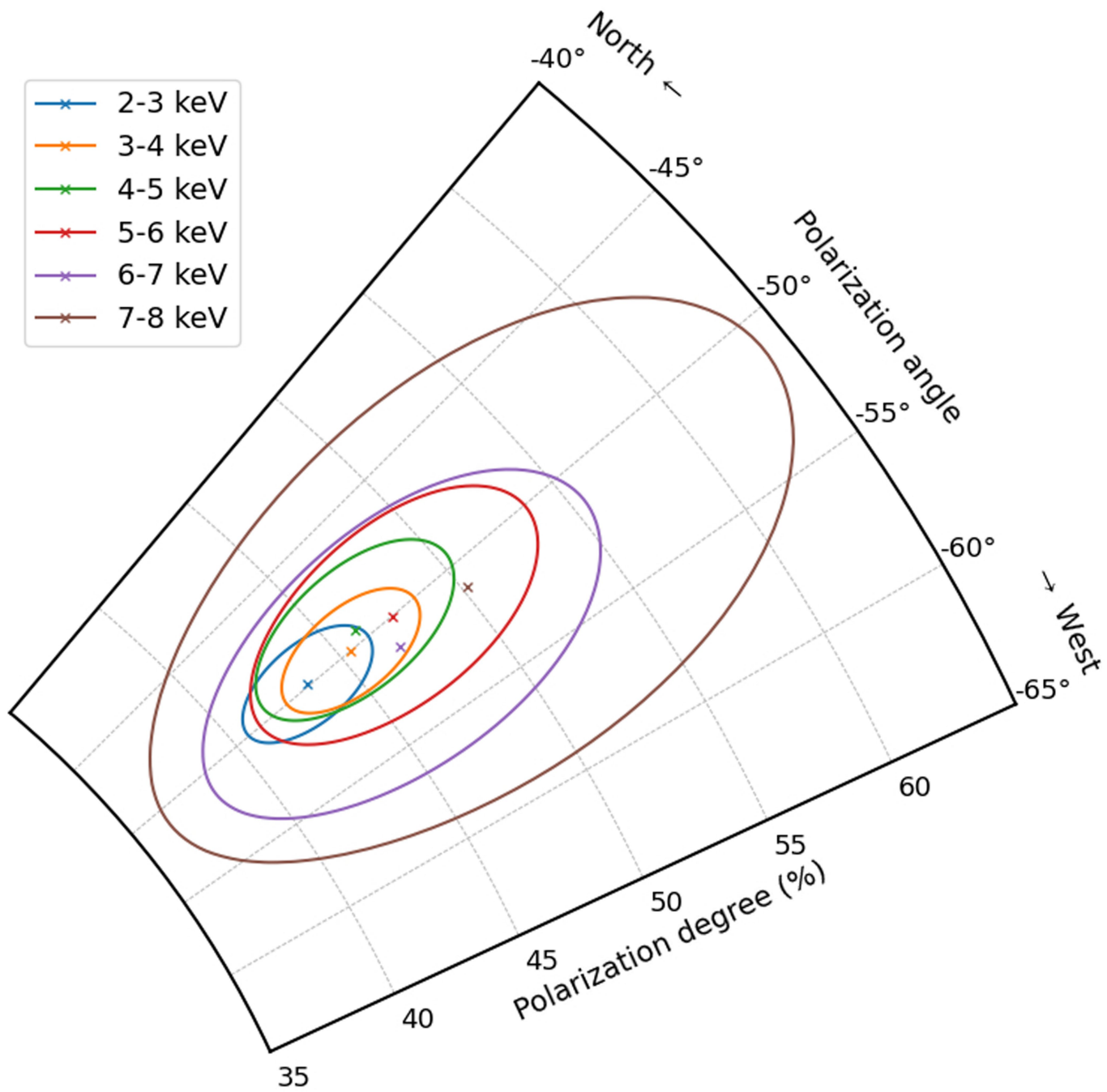


Extended Data Fig. 2 | Total nebula source (white 1' radius circle) and background (blue annulus, inner radius 2', outer radius 4.7') regions shown on images from DU1 (left) to DU3 (right). Intensity is on a logarithmic scale to bring out the faint background.

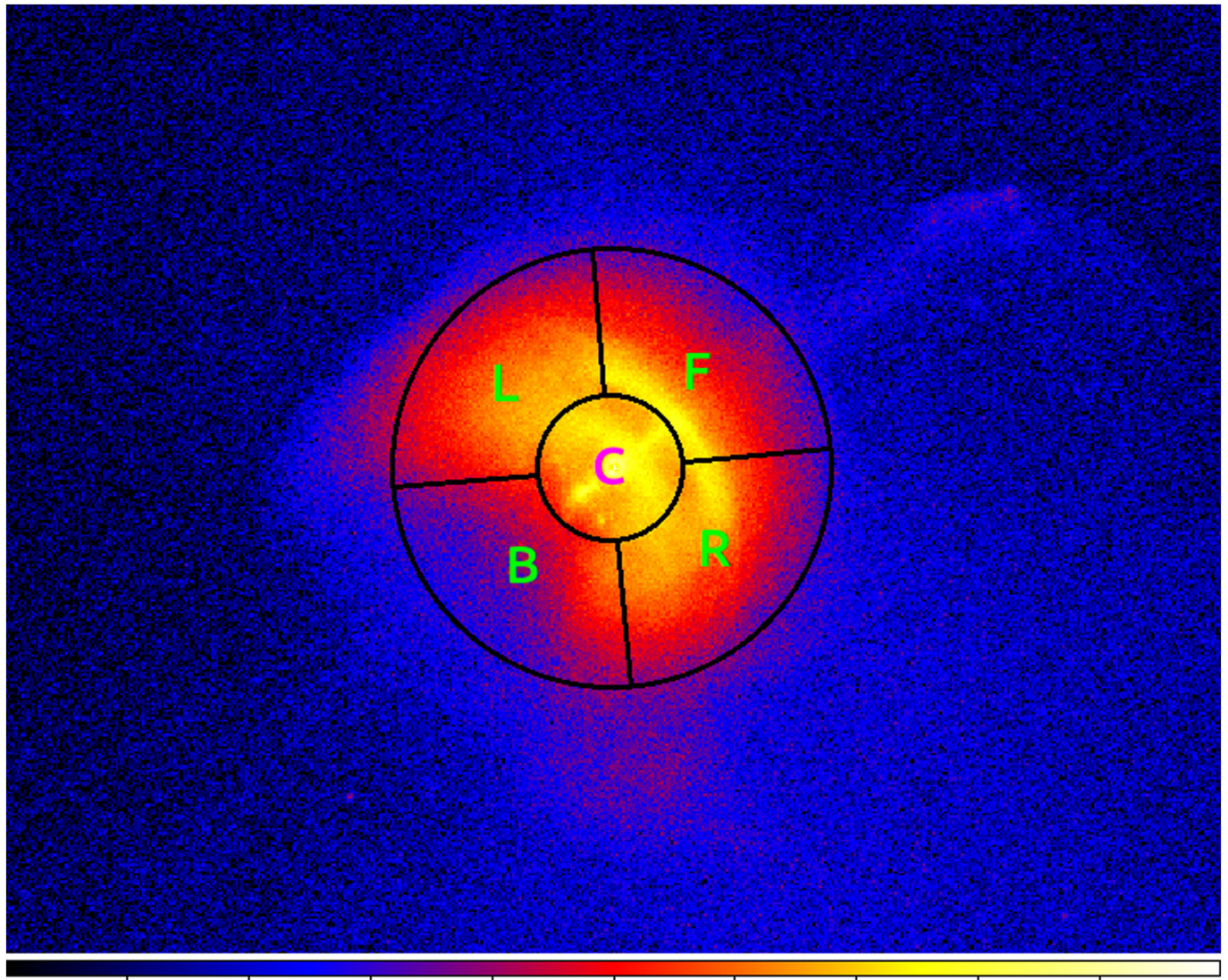


Extended Data Fig. 3 | Spectral joint fitting for the Stokes parameters in the 2–8 keV energy band for the three DUs using model TBABS*POWERLAW*POLCONST with previously fit spectral parameters fixed. The average

background count / spectrum for the three DUs is shown in black. Fit residuals are shown at the bottom.

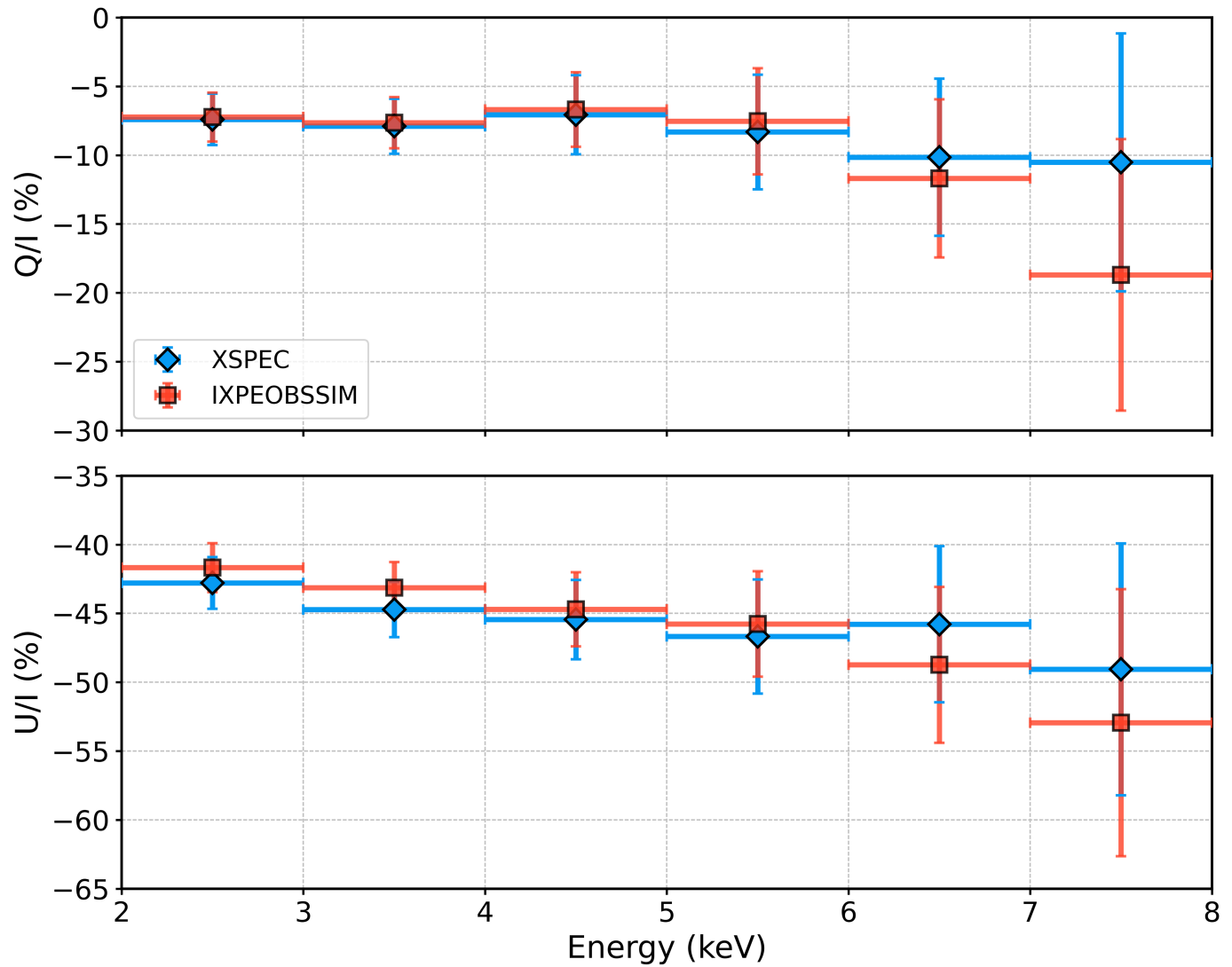


Extended Data Fig. 4 | Polar plot showing the polarization degree (PD) and polarization angle (PA) fit with data from the three DUs, for different energy bands. Ellipses show the 68.3% confidence level errors obtained with XSPEC.



Extended Data Fig. 5 | An alternative spatial partition of the PWN with regions aligned with the PWN symmetry axis on image observed by Chandra. *L, R, F, B* label the left, right, front, back regions with respect to the

C centre region respectively, corresponding to the analysis tabulated in Extended Data Table 4. The inner circle has a radius of 15'' and the outer circle radius is 45''.



Extended Data Fig. 6 | Q/I (top) and U/I (bottom) Stokes parameters of the Vela PWN as functions of energy in 2–8 keV range derived with *ixpeobssim* and XSPEC independently. The results are from the joint analysis of three DUs.

Extended Data Table 1 | Polarization degree and angle in six different energy bands and in the full IXPE 2–8 keV band

	2–3 keV	3–4 keV	4–5 keV	5–6 keV	6–7 keV	7–8 keV		2–8 keV
PD (%) ^I	42.3±1.8	43.8±1.9	45.2±2.7	46.4±3.8	50.1±5.7	56.1±9.7		44.6±1.4
PD (%) ^X	43.4±1.9	45.4±2.0	46.0±2.9	47.4±4.1	46.9±5.7	50.2±9.2		44.9±1.1
PA (°) ^I	−49.9±1.2	−50.0±1.2	−49.3±1.7	−49.7±2.4	−51.7±3.3	−54.7±5.0		−50.0±0.9
PA (°) ^X	−49.9±1.2	−50.0±1.3	−49.4±1.8	−50.0±2.5	−51.2±3.5	−51.1±5.4		−50.0±0.7

Polarization degree and polarization angle measured using *ixpeobssim* and XSPEC in six energy bands and 2–8 keV using three DUs. Uncertainties on the polarization degree and angle are calculated for a 68.3% confidence level, assuming that they are independent. The values from the two different methods are compatible within the uncertainties.

^IValues are obtained with *ixpeobssim*.

^XValues are obtained with XSPEC.

Article

Extended Data Table 2 | The normalized Stokes parameters and the detection significance within the bins of Fig. 1

	-2 ^b	-1 ^b	0 ^b	1 ^b	2 ^b	
2 ^a	0.33±0.17	0.20±0.13	0.07±0.11	-0.09±0.13	-0.14±0.15	Q/I ^c
	-0.18±0.18	-0.18±0.13	-0.61±0.11	-0.36±0.13	-0.45±0.14	U/I ^d
	1.3	1.2	5.0	2.0	2.6	Sig ^e
1 ^a	0.32±0.10	0.34±0.05	0.05±0.04	-0.10±0.07	-0.21±0.13	Q/I ^c
	0.07±0.10	-0.34±0.05	-0.53±0.04	-0.56±0.07	-0.42±0.13	U/I ^d
	2.5	9.7	12.9	7.6	3.1	Sig ^e
0 ^a	0.10±0.09	0.13±0.04	-0.09±0.02	-0.19±0.04	-0.08±0.11	Q/I ^c
	-0.03±0.09	-0.32±0.04	-0.48±0.02	-0.60±0.04	-0.43±0.11	U/I ^d
	-	8.8	19.7	15.6	3.3	Sig ^e
-1 ^a	-0.01±0.12	-0.20±0.07	-0.30±0.04	-0.44±0.05	-0.18±0.12	Q/I ^c
	-0.20±0.12	-0.19±0.07	-0.53±0.04	-0.37±0.05	-0.40±0.12	U/I ^d
	0.8	3.2	9.6	10.5	3.0	Sig ^e
-2 ^a	-0.07±0.15	0.04±0.13	-0.35±0.09	-0.42±0.11	-0.13±0.13	Q/I ^c
	-0.33±0.15	-0.01±0.13	0.05±0.09	-0.09±0.12	-0.11±0.13	U/I ^d
	1.4	-	3.1	3.2	0.1	Sig ^e

^a The row number where 0 presents the centre bin containing the pulsar.

^b The column number where 0 presents the centre bin containing the pulsar.

^c The Q/I Stokes parameters with 68.3% confidence level error.

^d The U/I Stokes parameters with 68.3% confidence level error.

^e The significance (σ) for the non-polarized hypothesis test, based on the standard normal distribution. The corresponding P value means the probability that a polarized signal is generated by a non-polarized source. Specifically, a significance of 2σ means that the probability that the emission is polarized reaches 95%. Conventionally, the minimum detectable polarization at 99% confidence level (MDP_{99}) corresponds to a significance of 2.33σ .

-No significant polarization detection.

Extended Data Table 3 | The Polarization degree and angle within the bins of Fig. 1

	-2 ^b	-1 ^b	0 ^b	1 ^b	2 ^b	
2^a	37±18	27±13	61±12	37±13	47±15	PD ^c
	-14±14	-21±14	-41.7±5.3	-52±10	-53.8±8.9	PA ^d
1^a	33±10	48.5±5.0	53.5±4.1	56.8±7.1	47±13	PD ^c
	6.3±9.0	-22.4±3.0	-42.2±2.2	-50.2±3.6	-58.2±7.7	PA ^d
0^a	10.3±8.8	34.4±3.9	49.0±2.5	62.8±4.0	44±11	PD ^c
	-7.4±24	-34.3±3.3	-50.3±1.5	-53.9±1.9	-50.5±7.4	PA ^d
-1^a	21±12	27.5±7.2	38.5±4.0	57.1±5.4	44±12	PD ^c
	-47±17	-68.3±7.5	-70.0±3.0	-69.8±2.7	-57.3±7.9	PA ^d
-2^a	34±15	4.5 ⁺¹³ _{-4.5}	34.9±9.5	43±12	17±14	PD ^c
	-51±13	-6.0±85	86.1±7.8	-84.2±7.6	-70±23	PA ^d

Polarization degree and polarization angle measured using *ixpeobssim*. Uncertainties on the polarization degree and angle are calculated for a 68.3% confidence level, assuming that they are independent.

^a The row number where 0 presents the centre bin containing the pulsar.

^b The column number where 0 presents the centre bin containing the pulsar.

^c The polarization degree (%) with 68.3% confidence level error.

^d The polarization angel (°) with 68.3% confidence level error.

Article

Extended Data Table 4 | The polarization degree and angle in the five regions shown in Extended Data Fig. 5

	Center [C]	Front [F]	Right [R]	Left [L]	Back [B]
PD (%) ^S	49.6±2.5	70.0±3.6	56.0±3.1	42.0±3.0	33.3±3.6
PD (%) ^{S+B}	48.8±2.5	65.4±3.6	53.1±3.1	39.9±3.0	31.1±3.7
PA (°) ^S	−50.2±1.5	−48.8±1.5	−64.9±1.6	−30.1±2.1	−59.4±3.1
PA (°) ^{S+B}	−50.3±1.5	−48.8±1.6	−64.9±1.7	−30.2±2.2	−59.4±3.4

Polarization degree and polarization angle in C, F, R, L, and B regions measured using *ixpeobssim* with and without background subtraction. Background regions are the same as shown in Extended Data Fig. 2. Uncertainties on the polarization degree and angle are calculated for a 68.3% confidence level, assuming that they are independent.

^S Values are obtained with background subtraction.

^{S+B} Values are obtained without background subtraction.